Author/s:
Barzegaramiriolya, M;Grant, ES;Ralph, T;Li, Y;Thalassinos, G;Tadich, A;Thomsen, L;Ohshima, T;Abe, H;Dontschuk, N;Stacey, A;Mulvaney, P;Hall, LT;Reineck, P;Simpson, DA

Title:
Functionalized Fluorescent Nanodiamonds with Millisecond Spin Relaxation Times

Date:
2025-10-28

Citation:
Barzegaramiriolya, M., Grant, E. S., Ralph, T., Li, Y., Thalassinos, G., Tadich, A., Thomsen, L., Ohshima, T., Abe, H., Dontschuk, N., Stacey, A., Mulvaney, P., Hall, L. T., Reineck, P. & Simpson, D. A. (2025). Functionalized Fluorescent Nanodiamonds with Millisecond Spin Relaxation Times. ACS Nano, 19 (42), pp.36884-36895. https://doi.org/10.1021/acsnano.5c02407.

Persistent Link:
https://hdl.handle.net/11343/367794

ACS NANO

www.acsnano.org

ARTICLE

Functionalized Fluorescent Nanodiamonds with Millisecond Spin Relaxation Times

Mina Barzegaramiriolya,[$] Erin S. Grant,[$] Trent Ralph, Yang Li, Giannis Thalassinos, Anton Tadich, Lars Thomsen, Takeshi Ohshima, Hiroshi Abe, Nikolai Dontschuk, Alastair Stacey, Paul Mulvaney, Liam. T. Hall, Philipp Reineck, and David A. Simpson*

Cite This: *ACS Nano* 2025, 19, 36884−36895

Read Online

ACCESS | Metrics & More | Article Recommendations | Supporting Information

ABSTRACT: **Fluorescent nanodiamonds (FNDs) containing nitrogen-vacancy (NV) defects are useful probes for biological imaging and nanoscale sensing applications. Here, we explore the effect of chemical surface modifications and core−shell structures on the T_1 relaxation times of 100 nm FNDs hosting nitrogen-vacancy ensembles. The results show that surface oxidation and silica coating of FNDs using the Stöber method can dramatically increase the spin relaxation time from $T_1 = 320 \pm 9$ μs to $T_1 = 1.00 \pm 0.06$ ms. Using FT-IR and NEXAFS measurements conducted on air oxidized particles, we find that changes to surface functional groups and sp^2 carbon density may be responsible for the observed enhancements to the spin relaxation rate. Finally, we use a Monte Carlo model to numerically investigate the relationship between chemical sensitivity and shell thickness and find that a shell thickness on the order of 1 nm should provide the highest sensitivity. Our findings demonstrate that the surface of FNDs can be engineered to exhibit bulk-like T_1 relaxation times, in the absence of complex quantum control sequences, which is crucial to advancing biosensing and imaging applications where surface spin noise currently limits measurement precision.**

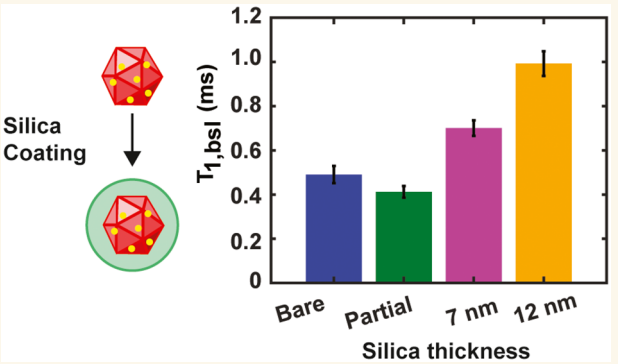

KEYWORDS: *fluorescent nanodiamonds, silica shell, nitrogen-vacancy center, T_1 relaxometry*

1. INTRODUCTION

Quantum sensing for the nanoscale detection of molecular and cellular processes using nitrogen vacancy (NV) defects in nanodiamond is an active area of research which has attracted marked attention.[1−5] The negatively charged nitrogen-vacancy defect is an atomic sized defect in diamond that can be optically excited using 532 nm light (see Figure 1A and B). The biocompatibility of diamond and photostable NV fluorescence can be used for long-term 3D bioimaging and tracking applications.[6] The electronic properties of the NV defect also provide a versatile sensing platform that can be used to measure local changes in physiochemical parameters such as magnetic field,[7] redox states,[8−11] temperature,[12−16] pH,[17,18] and electric potential.[19] Given the relevance of these quantities to biology, there have been an increasing number of sensing applications with FNDs in living systems.[20−23] These sensing experiments are performed using distinct measurement protocols. One of these, T_1 relaxometry, measures fluctuating magnetic fields at GHz frequencies that are produced by magnetic targets such as redox state changes,[11] paramagnetic molecules,[17,24−26] oxidative stress,[11,27,28] and polymer degradation.[29]

T_1 relaxometry using FNDs measures the rate of longitudinal spin relaxation out of a polarized NV ground state. Figure 1B) shows the relevant electronic energy structure of the NV defect in diamond, which consists of ground triplet and excited states. In the absence of an external static magnetic field, the ground state is a two-level system consisting of $m_s = 0$ and ± 1 spin sublevels. These are separated by a zero-field splitting of $D = 2.87$ GHz. The NV spin can be polarized into the ground $m_s = 0$ state using a green laser and its spin state can be read out optically via the intensity of the red fluorescence emitted. Local magnetic noise that overlaps with D induces faster spin relaxation out of the polarized state, which can be determined

Received: February 10, 2025
Revised: September 29, 2025
Accepted: September 30, 2025
Published: October 17, 2025

https://doi.org/10.1021/acsnano.5c02407
ACS Nano 2025, 19, 36884−36895

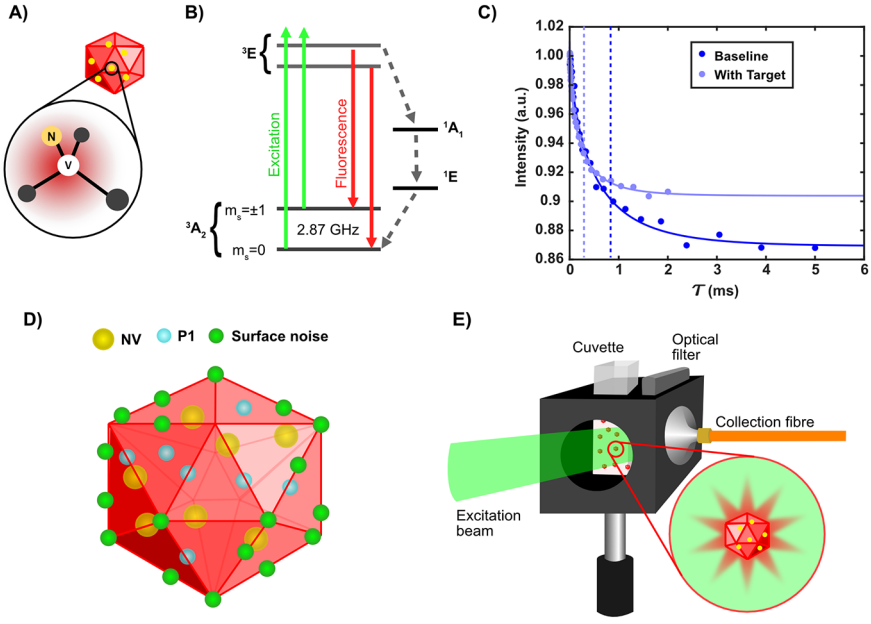

Figure 1. An overview of the NV defect andT_1 relaxometry. A) The NV defect consists of a substitutional nitrogen atom and an adjacent lattice vacancy. B) It behaves similarly to an isolated atom, with energy levels that includes ground and excited spin triplet states. The NV defect can be polarized into the ground $m_s = 0$ sublevel (bright state), which is separated from the $m_s = \pm 1$ sublevels (dark states) by a 2.87 GHz zero-field splitting. T_1 relaxometry probes the effect of on-resonance spin noise which increases the rate of relaxation out of the $m_s = 0$ polarized ground state. This spin relaxation process is read-out optically via the spin dependent NV fluorescence, as shown in C). External spin noise reduces the spin relaxation time (T_1) as shown by the light blue curve (with target) versus the dark blue curve (baseline). D) Each FND contains an ensemble of NV defects, shown in yellow. Internal magnetic noise sources such as additional substitutional nitrogen, known as P1 centers, and surface-localized spin noise species, both contribute to the (baseline) T_1 relaxation time. E) The measurement apparatus for in-solution T_1 relaxometry involves a cuvette to hold a small volume of suspended FNDs to which a target analyte can be added for sensing measurements.[2]

via the T_1 relaxation protocol.[30] Figure 1C shows an example T_1 relaxation curve from a baseline measurement (dark blue). The measured baseline relaxation rate, $\Gamma_{bsl} = {}^1/_{T_1}$, is governed by additive relaxation rates. These come from spin-phonon processes and inherent paramagnetic sources internal to the FND, Γ_{bulk}, surface spins, Γ_{surf}, and environmental spins that may be present in aqueous solutions, Γ_{env}. The addition of external paramagnetic target spins induces an extra relaxation term, Γ_{targ}, resulting in faster overall relaxation, (light blue curve in Figure 1C)). The sensitivity of T_1 relaxometry to external targets $\Gamma_{bsl} = \Gamma_{bulk} + \Gamma_{surf} + \Gamma_{env}R$, and C depends on several factors, however, Γ_{bsl} plays a critical role in determining both the magnetic sensitivity and dynamic range. It is therefore important to find new approaches to lower the intrinsic T_1 relaxation rates of FNDs. A recent study by March et al.[31] have shown that single NV defects in isotopically purified nanodiamonds with low nitrogen concentration (0.15 ppm), can result in T_1 relaxation rates of order 232 Hz (T_1 = 4.3 ms). In another study, Oshimi et al.[32] showed at higher nitrogen concentrations (30−60 ppm), isotopically purified nanodiamonds hosting NV ensembles show an average T_1 relaxation rate of 1470 Hz (T_1 = 0.68 ms). However, commercially available high pressure high temperature (HPHT) nanodiamonds with nitrogen concentrations [N] > 100 ppm generally exhibits T_1 relaxation rates of ∼3000 Hz ($T_1 \approx 0.3$ ms), which is approximately a factor of 2−3 times less than the isotopically purified material and as a result, they perform less favorably.

One possible avenue for improvement, involves coherent driving of GHz noise to negate its influence on sensing measurements.[33] However, this introduces practical challenges, as the power required to coherently drive electron spins at GHz frequencies is prohibitive. This challenge is further exacerbated in fluid environments where the orientation of both parasitic and NV spins, with respect to the microwave driving field, is random and dynamic. Material improvements are a more direct option that can reduce Γ_{bsl}. Unfortunately, control over sources of magnetic noise within the interior of FNDs is somewhat limited, given the primary source of commercial quantities of this material is HPHT synthetic diamond. This material contains high concentrations of P1 centers (substitutional nitrogen, at levels [N] ∼ 100 ppm) that contribute magnetic spin noise.[34] Improvements to reduce magnetic spin noise include optimization of thermal annealing treatments following irradiation with high energy electrons,[35] protons,[36] neutrons[37] and/or other elements.[38] These treatments aim to convert P1 centers into negatively charged NV defects, lowering the overall concentration of parasitic nitrogen spins.

In addition, significant effort has been put into understanding magnetic noise at the surface of FNDs[39,40] as it has been shown that the surface chemistry of FNDs can impact the fluorescence and spin properties of NV defects.[39,41−44] For example, surface species such as sp^2 carbon, surface adsorbates, and surface-modified phonon coupling have been suggested as sources of deleterious spin noise[40,45−47] while termination with oxygen, nitrogen and fluorine-containing species has been shown to improve NV properties, including the spin relaxation rate.[41,48] However, despite significant work in this area, the specific surface functional groups which impact T_1 relaxation rates are yet to be definitively nailed down and removed. This

https://doi.org/10.1021/acsnano.5c02407
ACS Nano 2025, 19, 36884−36895

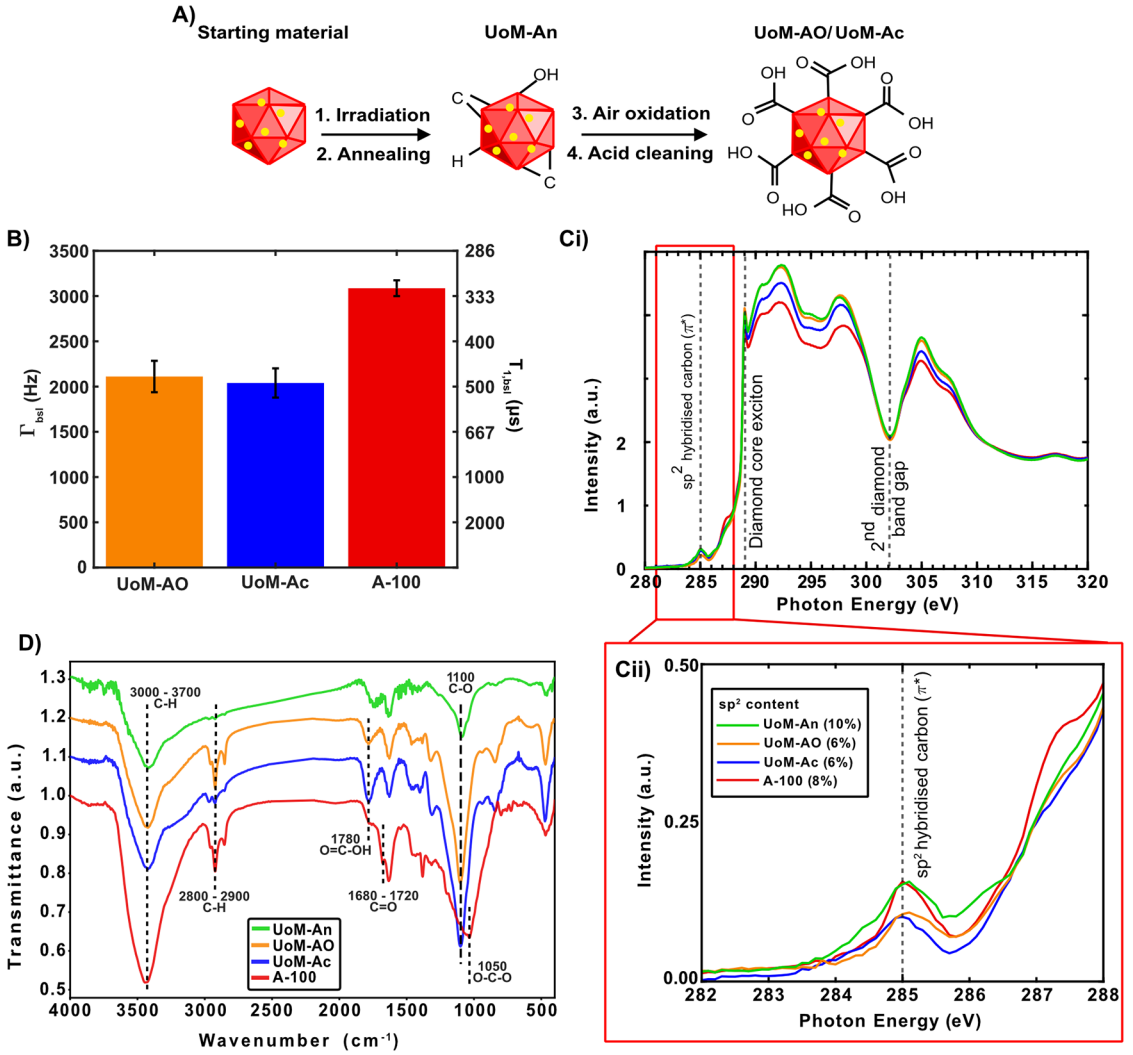

Figure 2. Analysis of the surface chemistry of the UoM and a commercial sample after purification, and their corresponding baseline T_1 relaxation rate. A) The FND purification process begins with nanodiamonds that have been irradiated with electrons to create vacancies in nitrogen-rich, HPHT starting material. These FNDs are then annealed to create NV defects (sample UoM-An), followed by oxidation in air (sample UoM-AO), and an acidification step (sample UoM-Ac). B) The baseline T_1 relaxation rate from of UoM-AO, UoM-Ac and a commercial sample of the same size (A-100, 100 nm diameter). Sample UoM-An did not provide a measurable T_1 relaxation curve. C) (i) NEXAFs spectra for the same samples. (ii) A zoom of the pre-edge region between 282 and 288 eV which shows the C═C peak at 285 eV. D) FT-IR spectra of each sample.

highlights the importance of understanding the impact certain moieties can have on the spin properties of NV defects.

As well as affecting T_1 relaxation rates, manipulation of the surface chemistry of FNDs can be crucial for biological applications and is frequently used to engineer specific binding to target biomolecules of interest.[49−52] Common functionalization strategies include conjugation with antibodies,[53] peptides,[54] and DNA.[55] Polymer coatings such as poly ethylene glycol (PEG), polyglycerol (PG), polydopamine (PDA) and poly(ethylene imine) (PEI) have been significantly used to improve the biocompatibility and colloidal stability of nanodiamonds, particularly for clinical and biomedical applications.[52] However, these coatings often create inhomogeneous, thick layers that increase the distance between NV centers within the nanodiamond and the target analyte, affecting the sensing performance. They also involve multistep synthesis and can introduce magnetic or dielectric interference.

In contrast, silica functionalization is one of the most common surface modification methods. Silica can maintain the stability of FNDs in suspensions across a range of pHs, as well as in aqueous and nonaqueous solutions due to the presence of silanol groups.[56] Silica coated nanoparticles are also biocompatible, nontoxic and resistant to microbial attack.[57] Silica is optically transparent, allowing efficient excitation and emission of fluorescence,[58] and silicon linkers are available with a variety of terminal groups including amin-, thiol-, methacrylate-, etc., affording covalent bonding with different targeting agents such as proteins, nucleic acids, antibodies, etc.[59−61] Although silica coating has been previously demonstrated using FNDs,[50,62−64] most work has assessed its utility only in terms of providing a suitable substrate for biological linkages and in providing geometric homogeneity.[60,63,64] One recent work,[65] undertaken concurrently to this investigation, showed that an 18 ± 2 nm silica coating improves both T_1 and T_2 times in individual FNDs. However, only 24 particles with one silica thickness were studied. As a complementary investigation, therefore, it is interesting to study the effect of silica coating on the entire ensemble of FNDs as well as the effect of shell thickness.

https://doi.org/10.1021/acsnano.5c02407
ACS Nano 2025, 19, 36884−36895

Fortuitously, Stöber synthesis is straightforward as well as being very sensitive to the concentrations of the reagents used, offering a way to tune the thickness of the silica shell. Additionally, we have recently presented a method for studying T_1 relaxometry on an ensemble of FNDs while they are dispersed in a solution, which we employ here.[30]

In this work, we manipulate the surface chemistry of FNDs to mitigate potential sources of magnetic noise in FND NV ensembles, as outlined in Figure 1D. We take advantage of our recently developed in-solution T_1 relaxometry method, which uses the apparatus shown in Figure 1E, to assess the FNDs produced.[30] Using this technique, we show that controlled surface termination and functionalization using silica encapsulation can produce bulk-like T_1 spin relaxation rates in 100 nm FNDs. Furthermore, we assess the potential source of this improvement using Fourier-transform infrared spectroscopy (FT-IR) and near-edge X-ray absorption fine structure (NEXAFS) spectroscopy. Finally, we measure the sensitivity of silica-coated FNDs in comparison to bare particles and consider, using a numerical model, the trade-off between improved Γ_{bsl} and increased standoff between the NV defects and a magnetic target.

2. RESULTS AND DISCUSSION

2.1. FND Surface Purification. Homogenizing the FND surface is an important first step prior to surface functionalization. This is particularly true in the case of silica functionalization, which requires homogeneous oxygen terminated surfaces.[63] Figure 2A) shows a flowchart of the surface treatment steps employed to homogenize the FND surface; three samples created, one after each step. The starting material was commercially available Type Ib HPHT nanodiamond (Microdiamant MSY 0−0.2) with a nominal particle diameter of 100 nm and nitrogen concentration [N] > 100 ppm. These nanodiamonds were irradiated with high energy electrons (2 MeV) at a fluence of 1×10^{18} electrons/cm^2 to produce lattice vacancies and then annealed (An) in vacuum at 800 °C for 4 h and 900 °C for 1h to produce NV defects (labeled sample University of Melbourne (UoM-An)). To ensure a purified nanodiamond surface, we implemented two consecutive steps: air oxidation (AO) (sample UoM-AO) and acid cleaning (Ac) (sample UoM-Ac). These steps aimed to remove metallic impurities, reduce the presence of amorphous carbon, and increase the concentration of carboxylic acid groups or oxygen functional groups.[52,66] The air oxidation step plays a crucial role and requires careful optimization to achieve a high percentage of oxygen on the nanodiamond surface. To optimize this process for our specific nanodiamond type, we conducted air oxidation at four different temperatures 540 °C, 550 °C, 565 °C, and 575 °C and analyzed the results using FT-IR. Detailed FT-IR results are provided in Figures S1 and S2 (refer to the Supporting Information). Based on these findings, we determined that oxidizing nanodiamonds at 565 °C for 3 h yielded the most optimized surface. It is important to note, however, that the time and temperature used in the air oxidation step should be carefully adjusted for different sizes and types of nanodiamonds. This is because it significantly influences the amount of carboxylic acid groups on the surface and the removal of sp^2 carbon, making it a critical aspect of the nanodiamond preparation process.

2.2. T_1 Relaxometry Measurements. To assess the efficacy of this purification procedure we first conducted T_1 relaxation measurements for the three samples (UoM-An, UoM-AO, and UoM-Ac). For comparison, a commercial sample with the same nominal diameter of 100 nm (labeled A-100) was obtained from Adamas Nanotechnologies. T_1 relaxation curves were acquired using a dispersed solution of each FND sample suspended in water at a concentration of 10 μg/mL. This approach mitigates potential bias associated with single-particle studies by ensuring thousands of FNDs are measured together.[30] Measurements were performed using a custom system shown in Figure 1E, centered on a cuvette which holds 190 μL of FNDs, suspended in purified water. Pulsed optical excitation at 532 nm was achieved using an acousto-optical modulator and the resulting NV fluorescence was collected into a multimode fiber positioned at 90° to the illumination and detected with a single photon avalanche photodiode. See methods for further information.

Figure 2B shows the average value of the T_1 relaxation rate, Γ_{bsl}, from three of the four samples. UoM-An did not provide a measurable T_1 decay curve despite producing sufficient fluorescence (roughly half the fluorescence of UoM-AO). We attribute this to the fact that the UoM-An sample has amorphous carbon on the surface which resulted in significant autofluorescence preventing the T_1 relaxation curve from being obtained. Both the UoM-AO and UoM-Ac samples did provide measurable T_1 relaxation rates with the UoM-AO exhibiting a $\Gamma_{bsl} = 2100 \pm 200$ Hz ($T_1 = 470 \pm 40$ μs) and UoM- Ac a rate of $\Gamma_{bsl} = 2040 \pm 80$ Hz ($T_1 = 490 \pm 20$ μs). In contrast, the commercial A-100 sample had a factor of 1.5 times faster T_1 relaxation rate; $\Gamma_{bsl} = 3130 \pm 90$ Hz ($T_1 = 320 \pm 9$ μs). To elucidate the potential cause of these differences FT-IR and NEXAFS were performed on all four samples.

2.3. Near Edge X-ray Absorption Fine Structure (NEXAFS). To understand the impact that air-oxidation and acidification have on the surface of the FNDs we applied two characterization methods to the samples. To begin, we measured NEXAFS spectra collected at the carbon K-edge. NEXAFS measurements were executed in total electron yield (TEY) mode, probing approximately the top 10−20 nm of each sample.[67] In Figure 2C(i) and (ii), the carbon K-edge spectra for all UoM and Adamas samples are presented, revealing distinct features in the pre-edge region (282−288 eV). All samples exhibit a peak at 285 eV, associated with the π^* orbital of sp^2-hybridized carbon. The percentage of sp^2 carbon can be quantified from this peak using a pure sp^2 reference sample (refer to methods) via the expression:

$$sp^2\ [\%] = \frac{I_s^{\pi^*}/I_s^{\sigma^*}}{I_{ref}^{\pi^*}/I_{ref}^{\sigma^*}} \times 100 \quad (1)$$

where I^{π}*is the peak area of the π^* peak at 285 eV and I^{σ}* is the integrated σ^* resonance signal between 289.0 and 320 eV. Subscripts 's' and 'ref' refer to the sample and highly oriented pyrolytic graphite (HOPG) reference material. The sp^2 carbon content was determined to be ∼10% for UoM-An, ∼6% for both the UoM-AO and UoM-Ac samples, and ∼8% for A-100. Although these differences correlate with the T_1 relaxation rates measured for each sample, estimations of sp^2 content via NEXAFS data may be subject to errors of up to 20%,[68] so it is not clear from these results that sp^2 content is the sole influence on the relaxation rates of FNDs.

While samples UoM-AO and UoM-Ac provided relatively similar NEXAFS spectra in the pre-edge region, the UoM-An and A-100 samples showed features in addition to the peak at 285 eV. The spectra collected from Sample A-100, has a small

https://doi.org/10.1021/acsnano.5c02407
ACS Nano 2025, 19, 36884−36895

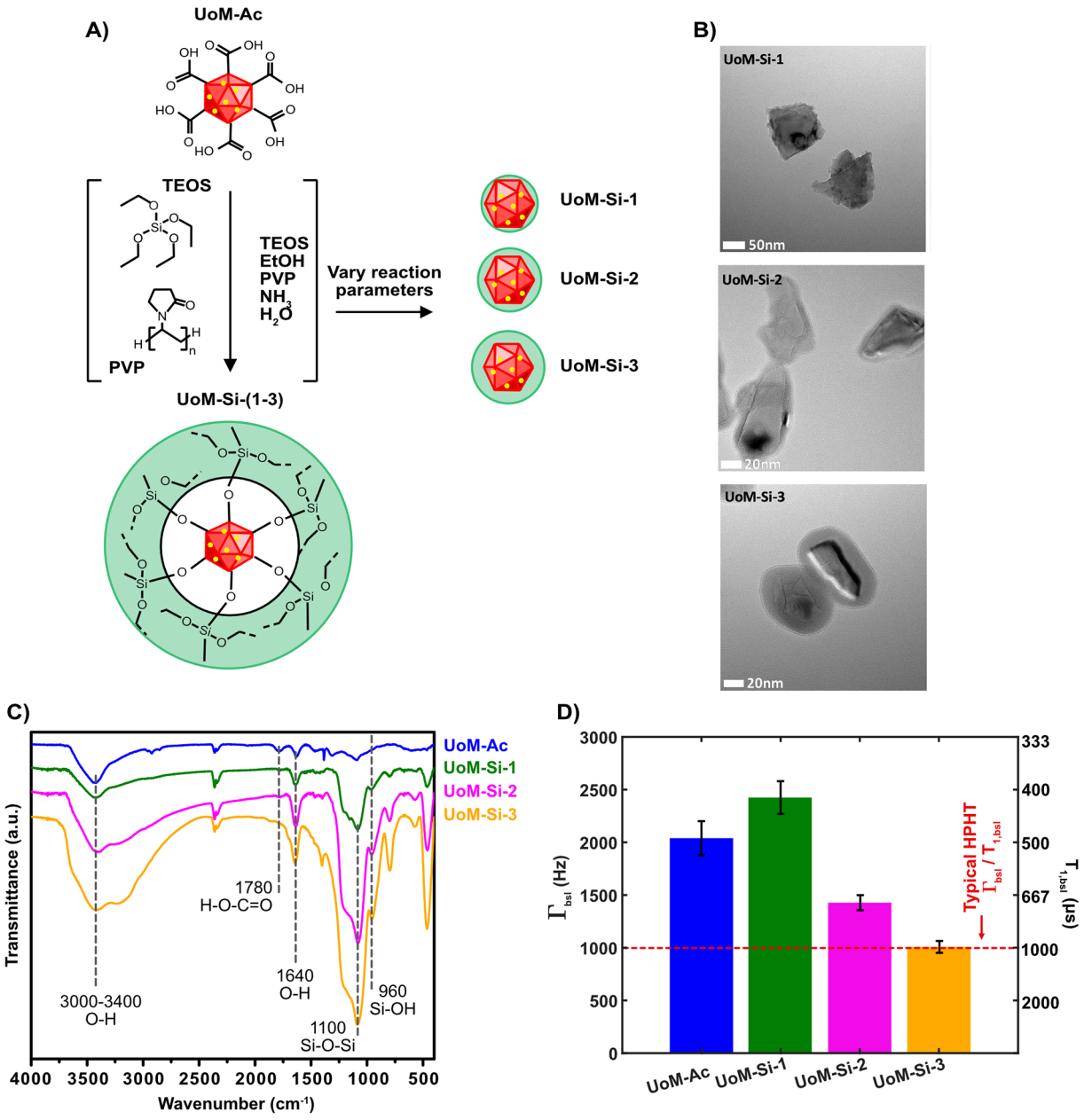

Figure 3. TEM images, FTIR and T_1 results of each silica-coated sample. A) UoM-Ac particles are treated with the Stöber process to produce FNDs coated in a silica shell. The parameters that make up the Stöber process are varied such that the final thickness of the silica shell can be tuned. B) TEM images of UoM-Si-(1−3). A silica shell can be seen surrounding the samples that underwent the Stöber process. These samples also show a difference in shell thickness. C) FT-IR spectra for all silica coated UoM samples. There are distinct peaks in the samples that underwent the Stöber process. For example, there is a peak at approximately 1100 cm^{-1} which corresponds to Si−O−Si, 960 cm^{-1} corresponding to Si−OH and ~3400 cm^{-1}, which may indicate water hydrogen bonded to silanol. Together, these peaks confirm the successful application of silica to these particles through the Stöber process. D) Γ_{bsl} for the silica-coated particles compared to UoM-Ac. For UoM-Si-2 and UoM-Si-3 which both have complete silica shells, there is a large improvement in the relaxation rate. UoM-Si-3 has Γ_{bsl} commensurate with typical HPHT bulk diamond.

peak at 287.5 eV which is typically associated with C−H bonding.[68] Sample UoM-An on the other hand, displays features to either side of 285 eV. This sample was visibly black in color and did not disperse well, indicating the presence of amorphous or mixed phase sp^2/sp^3 carbon produced by the annealing process. This is supported by additional unresolved peaks near 284 and 286 eV which suggest the presence of further unoccupied states within the diamond bandgap. These added electronic states are deleterious for the negative charge state of the NV defect,[46] and will contribute to the lower NV fluorescence of the UoM-An sample. Upon air-oxidation, the FNDs become white, are easily dispersed in Milli-Q water and these additional NEXAFS features disappear, showing the air-oxidation process removes this contaminating carbon material, as desired.

2.4. Fourier-Transform Infrared Spectroscopy (FT-IR).

The FT-IR results, displayed in Figure 2D, provide information about the functional groups present on the surfaces of each UoM and A-100 sample. Interestingly, while the UoM-AO and UoM-Ac samples show a peak at 1780 $cm^{-1,}$ corresponding to

https://doi.org/10.1021/acsnano.5c02407
ACS Nano 2025, 19, 36884−36895

Table 1. Reaction Parameters and Results of DLS and TEM Analysis of the Silica Shell Thickness for All Three UoM-Si Samples and the Starting Material

FND	TEOS	Ammonia	PVP	Water	DLS(Z-average)	DLS (PdI)	TEM (Shell thickness)
UoM-Ac					127 ± 1.3 nm	0.133 ± 0.06	
UoM-Si-1	40 μL	250 μL	96 mg	0.4 μL	154 nm	N/A	3 ± 1.6 nm
UoM-Si-2	80 μL	250 μL	96 mg	0.1 μL	160 ± 10 nm	0.290 ± 0.07	6 ± 2 nm
UoM-Si-3	80 μL	250 μL	96 mg	0.4 μL	268 ± 5 nm	0.210 ± 0.07	11 ± 2 nm

HO−C═ O (C═O stretching), the A-100 sample appears to have an extra peak around 1680−1720 cm^{-1} which is an indication of carbonyl groups in ketones or aldehydes (C═O stretching).[69] The A-100 sample also does not have a sharp peak at 1100 cm^{-1} like the UoM samples, but instead shows a broad peak from 900-1200 cm^{-1}. The broad peak at lower wavenumbers may include the primary alcohol stretch at 1100 cm^{-1} as well as a peak between 1150 and 1050 cm^{-1} from C−O−C.[70]

In contrast, UoM-AO and UoM-Ac samples show narrow peaks at 3300 cm^{-1}, 1780 cm^{-1}, and 1100 cm^{-1}, indicating more defined oxygen bonding environments. Interestingly, these results also suggest that the additional acidification step, performed on the UoM-Ac sample, did not significantly change the FND surface. This is in line with the observed values of Γ_{bsl} in Figure 2B, which were similar for both UoM-AO and UoM-Ac samples. However, previous studies show that acidification is a necessary step in the fabrication protocol as it ensures good colloidal stability and removes metallic impurities from the surface which may not be evident in the FT-IR spectrum.[71,72]

In combination, the FT-IR results suggest that the in-house oxidation and acid cleaning steps performed on the UoM samples have resulted in a more homogeneous collection of functional groups than were found on the A-100 sample. This could be an important factor which contributes to the differences in Γ_{bsl} obtained for the UoM and A-100 samples. However, we note that the fluorescence intensity from the A-100 sample is approximately a factor of 10 greater than the UoM samples. This is likely the result of a higher irradiation dose which enables the creation of a higher density of NV defects. Therefore, it is difficult to interpret whether the measured Γ_{bsl} differences are surface-induced or due to differences in bulk spin noise which can arise during irradiation and annealing via the formation of vacancy pairs. To investigate the potential role of the surface, we functionalized the UoM material with silica and studied the impact on the T_1 relaxation rate. In this case, the bulk spin properties of the FNDs remain consistent and any surface related effects can be evaluated.

2.5. Silica Encapsulation. The T_1 results demonstrated by the oxidized UoM samples are above average for commercial FNDs,[73] however Γ_{bsl} is still a factor of 1.5 times larger than the T_1 relaxation rates reported for isotopically purified FND ensembles− approximately 1400 Hz (equivalent T_1 of ∼700 μs).[32] We investigated whether the introduction of silanol groups, via silica coating, could provide an enhancement. Silica coating was limited to the UoM-Ac sample, as A-100 material is supplied dispersed in water, at a concentration too low for use in functionalization experiments.

Despite exploring a small portion of the available parameter space of the Stöber synthesis protocol (see Materials and Methods), we were able to generate three distinct samples with different shell thicknesses, labeled UoM-Si-(1−3), as shown in Figure 3A. The silica shell produced in each sample was assessed in terms of its hydrodynamic radius using dynamic light scattering (DLS), actual thickness at a single particle level using transmission electron microscopy (TEM), and chemical composition of the surface using FT-IR.

Table 1 presents the reaction parameters and outcomes of the DLS and TEM measurements. DLS results indicate that samples UoM-Si-(1−3) possess silica shells of increasing thickness, each exhibiting a larger hydrodynamic radius than the UoM-Ac starting material. Corroborating these findings, the TEM images (Figure 3B) offer detailed insights into the exact thickness and uniformity of the shells. The top image displays UoM-Si-1, generated using 40 μL of tetraethyl orthosilicate (TEOS), 250 μL of ammonia (NH_3), and 96 mg of polyvinylpyrrolidone (PVP, MW 10,000). This sample exhibits an incomplete silica coating, with a thickness of 3 ± 1.6 nm in the places where silica was found, due to insufficient material to cover all FNDs in the sample. UoM-Si-3 was produced by increasing the amount of TEOS, which resulted in continuous silica shells with a thickness of approximately 11 ± 2 nm, as depicted in the TEM images. For sample UoM-Si-2, the amount of water was decreased, and the amounts of both TEOS and NH_3 remained unchanged compared to UoM-Si-3. This condition led to a homogeneous silica shell on the FND surface, with a thin layer of silica (6 ± 2 nm), as determined by TEM measurements. The thickness of the silica shell from the TEM images was determined by taking line cuts of the silica in ImageJ and averaging the data. In the case of the UoM-Si-1 sample, 196 individual line cuts were taken, spread across 46 nanodiamonds. UoM-Si-2 had 277 line cuts, spread over 89 nanodiamonds, and UoM-Si-3 had 186 line cuts spread over 28 nanodiamonds. All TEM images are depicted in Figures S4−6 of the Supporting Information. It is important to note that this paper does not explore the full scope of the parameter space for Stöber synthesis. If the parameter space was mapped, however, it may identify avenues to achieve tailored silica shell thicknesses. This type of study is beyond the scope of the current work.

FT-IR spectra of the UoM-Ac and silica coated FNDs was used to corroborate the DLS and TEM results and are depicted in Figure 3C. The peaks at ∼960 and 1100 cm^{-1} are due to the Si−OH stretching vibration and Si−O−Si stretching respectively.[69] The broad peak at ∼3500 cm^{-1} is due to the overlap of both OH stretching bands of hydrogen bonded water molecules and SiO−H stretching of surface silanols hydrogen-bonded to molecular water.[74] The signal at 1780 cm^{-1}, on the other hand, which is assigned to the C═O of the carboxylic acid peak in UoM-Ac, is not present in samples UoM-Si-2 and 3, indicating full coverage of the shell around each FND.

2.6. Comparisons of the Baseline T_1 Relaxation Rates. The intrinsic T_1 relaxation rates of each of the silica-coated samples were measured to determine the effect of the surface functionalization. Figure 3D shows that for UoM-Si-1, which does not have an intact shell, the T_1 relaxation rate is within the measurement error of the UoM-Ac sample, indicating that

https://doi.org/10.1021/acsnano.5c02407
ACS Nano 2025, 19, 36884−36895

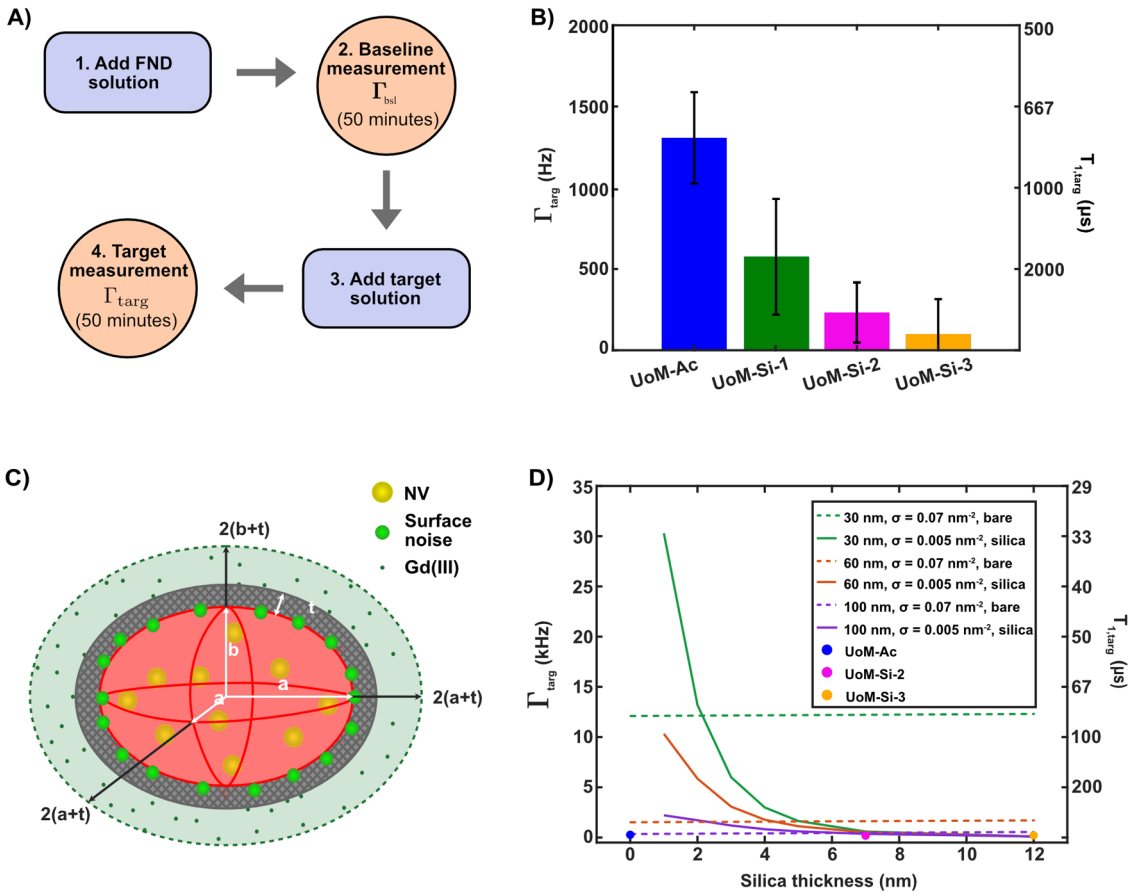

Figure 4. Experimental and theoretical studies of silica-coated FNDs. A) The sensing protocol. B) Γ_{targ} for the silica coated particles compared to UoM-Ac. It is clear that the sensitivity decreases once silica is added. C) The sensing simulation consists of ellipsoidal FNDs with two equal major axes *a* and a third axis *b*. The silica shell is added as an empty buffer region of variable thickness. This is surrounded by a final ellipsoidal volume with major axes of 2(a+t) and 2(b+) containing Gd(III) ions. The fluorescence resulting from each NV defect in each of the 5000 simulated FNDs is summed, to give the measured fluorescence intensity. D) Results of the simulation for FNDs with a = 30, 60, and 100 nm. Dotted lines show Γ_{targ} for bare particles with a surface noise density of 0.07 nm^{-2}, while the solid lines show Γ_{targ} for silica coated particles of increasing shell thickness. Silica-coated particles have a reduced surface noise density of 0.005 nm^{-2}. Individual data points for UoM-Ac, UoM-Si-2, and UoM-Si-3 are also plotted for comparison.

a silica shell which is incomplete does not improve the T_1 relaxation rate. However, for samples with a continuous shell, there is a dramatic decrease in the T_1 relaxation rate. Sample UoM-Si-2, which has a 6 ± 2 nm shell has Γ_{bsl} = 1430 ± 71 Hz (T_1 = 700 ± 35 μs), close to that observed for isotopically engineered FNDs.[32] Once the shell is increased to 11 ± 2 nm, in UoM-Si-3, the T_1 relaxation rate reaches Γ_{bsl} = 1000 ± 60 Hz (T_1 = 1000 ± 60 μs), this equates to a factor of 2 increase in the T_1 relaxation time compared to the oxidized FNDs. The assembly of the silica shell was replicated on multiple FND batches, see Supporting Information (Table S1 and Figures S11−15), where we again observed consistent extensions in the baseline T_1.

It is worth noting that all-optical T_1 measurements can be difficult to interpret in situations where the NV charge state is modified over the duration of a measurement. However, in a previous study, we demonstrated that the all-optical T_1 protocol used here was not significantly impacted by *dynamic* charge state changes or diffusion of the FNDs in solution.[30] Another consideration for the analysis of Γ_{bsl}, is whether the observed decrease in Γ_{bsl} for the silica coated FNDs, comes from an overall, *static,* redistribution of NV charge states; converting NV^- to NV^0 near the FND surface. This would result in a T_1 time that is dominated by bulk NV^- defects that are less sensitive to surface noise sources. However, a recent study by Zvi et al. showed that NV^- fluorescence intensity in fact increases with silica coating by a few percent.[65] Therefore, charge state redistribution due to the silica coating is unlikely to be the reason we see an increase in the T_1 relaxation rate.

We propose that the improvement seen in the silica coated samples, UoM-Si-2 and UoM-Si-3, is due to passivation of surface noise. The baseline relaxation rate, Γ_{bsl}, is then limited by thermalization processes and internal noise sources, in the same way as bulk diamond. This conclusion is supported by Zvi et al., who showed that the T_1 time and spin dephasing time, T_2, of individual, 44 nm FNDs, was improved by silica coating. In combination with our work, it appears that silica-coating provides a wide bandwidth suppression of magnetic noise, in the MHz to GHz range. This suppression of surface noise demonstrates that FNDs have an adequate internal spin environment to support T_1 relaxation rates approaching those observed for near-surface NV ensembles in HPHT single crystal diamond.

It is interesting that Γ_{bsl} varies with the thickness of the silica shell, an effect that we also saw in additional batches. We expect that alterations to the surface noise density should be

https://doi.org/10.1021/acsnano.5c02407
ACS Nano 2025, 19, 36884−36895

independent of silica thickness once a uniform shell is established, however that is not what we observe. This difference could be caused by an inhomogeneous coverage of silica on the sample, wherein some particles are fully covered while others have very little coverage. However, if we consider the stretched exponential power, p (see Methods section), used in the fit to the T_1 data, we can see this is likely not the case. The UoM-Ac sample has a stretched exponential power of $p = 0.70 \pm 0.05$, whereas UoM-Si-2 and UoM-Si-3 both have $p = 0.80 \pm 0.04$. The power of the exponential fit is linked to the distribution of T_1 relaxation rates in the FND ensemble with a lower power indicative of a broader distribution. However, both the UoM-Si-2 and UoM-Si-3 samples exhibit powers close to 1 suggesting that in both cases there is a relatively narrow distribution of T_1 relaxation rates. This is corroborated by the TEM images, which show silica shells present on all FNDs (see Figures SI4−6).

The improvement in T_1 relaxation rate with silica thickness could also suggest that the silica is simply 'pushing away' a noise source external to the nanodiamond. To test one possible source of solution-based noise − dissolved molecular oxygen − we purged the UoM-Ac solution using nitrogen gas and measured the resulting T_1 relaxation rate. Following this, we reintroduced oxygen to the sample and measured again. There was no significant difference between these measurements, (see Figure S17). Therefore, dissolved molecular oxygen is unlikely to be the source of unwanted spin noise. Milli-Q water should not contain other sources of paramagnetism, so the reason for improved T_1 times with silica coating is not likely to be caused by simply moving the environment further away, although more work should be done to confirm this.

2.7. Sensing Using Spin Relaxometry. Although the introduction of a silica shell greatly improved the intrinsic T_1 relaxation rate of the UoM-Ac sample, it was important to test whether these particles also retain sensitivity to external magnetic targets when functionalized in this manner. The magnetic signal from magnetic targets scales as $\sim r^{-6}$, where r, is the distance between an NV defect and the target of interest. This dependence means that any increase in interaction distance could have a dramatic impact on the magnetic sensitivity and limit of detection of the FNDs. To test the sensing ability of the silica coated FNDs, we applied a target solution of gadobutrol monohydrate at 2.4 mM. As presented in a previous study,[30] gadobutrol is a useful benchmarking target because it provides a strong signal due to its 7 unpaired electron spins. It is also ionically stable, reducing potential signals arising from chemical interactions between the molecule and FNDs.

Sensing was conducted according to the protocol in Figure 4A. A baseline measurement of the T_1 relaxation rate in water provides Γ_{bsl}, which is then used in the fit of a second measurement after the addition of gadobutrol, to obtain Γ_{targ}. Details of the sensing protocol are provided in the Methods section. The results of the sensitivity study are presented in Figure 4B. The sensitivity of the silica-coated samples declines with increasing shell thickness, as expected, restricting the utility of these particles for paramagnetic sensing. These results suggest that each additional nanometer of separation between the NV defects, and the target molecule has a large impact on the sensitivity, making it important that shell thicknesses are kept as small as possible.

To get a better understanding of the relative relationship between shell thickness, FND size, and sensitivity, we developed a theoretical model to simulate the FND geometry, silica coating and the magnetic interaction between the NV ensemble and paramagnetic targets. The details of the Monte Carlo model used to capture the distribution of FNDs and NV properties inherent to an ensemble measurement are outlined in the SI. The model geometry and fit parameters are illustrated in Figure 4C.

The model simulated the resultant fluorescence signal from 5000 ellipsoidal FNDs. The FND geometry was chosen to reflect the recent evidence that FNDs are nonspherical and jagged, but nonetheless roughly ellipsoidal. Specifically, work by Eldemrdash et al.[75] showed that 90 nm FNDs from Adamas Nanotechnologies, which are very similar in size to the sample used here, had xy radii of 50 ± 10 nm and a z axis of 30 ± 5 nm. These dimensions were used to generate the ensemble of FNDs with dimensions normally distributed around these means. NV defects were then randomly positioned within the FNDs at a density of $\rho = 3$ ppm. For simplicity, and in the absence of data to support any other distribution, NV defects were allowed to exist at any point within the FND with equal probability. The effect of adding a silica shell was simulated by reducing the surface spin noise density, σ, compared to bare FNDs. The values of σ were chosen such that the simulated FNDs with 100 nm xy diameter had an intrinsic T_1 relaxation rate which matched the experimental data both with and without a silica shell. To accurately replicate the experimental results $\sigma = 0.07$ spins/nm^{-2} on the bare FNDs and 0.005 spins/nm^{-2} when a silica shell was applied.

Figure 4D shows a plot of Γ_{targ} for FNDs with xy diameters of 30, 60, and 100 nm. The dotted lines show each size with a surface noise density of $\sigma = 0.07$ spins/nm^{-2} and no silica shell, while the effect of the silica shell (starting at 1 nm thick) is shown by the solid lines. In this case the surface spin noise density is reduced to 0.005 spins/nm^{-2}. The experimental data acquired for UoM-Ac, UoM-Si-2 and UoM-Si-3 is also included, to compare the model results to those derived from experiment. These data points align well with the modeled results for 100 nm FNDs, as desired. UoM-Si-1 was excluded as it has an incomplete shell with a surface spin density approximately equal to the bare FNDs based on the measured T_1 relaxation rates.

The simulation shows that sensitivity, indicated by Γ_{targ}, is inversely correlated with both FND size and silica shell thickness. This is expected, as reducing either parameter will put more NV defects close to the external environment. Interestingly however, the sensitivity of each FND size is better when the silica shell is 1 nm, compared to the bare particle, as the estimated reduction in surface noise density produced by the silica compensates for the increase in standoff. Although the model contains too many independently unverifiable parameters, limiting the utility of the absolute values it provides, this result nevertheless suggests an optimal shell thickness exists and is likely on the order of a nanometer. A wider exploration of the parameter space of Stöber synthesis will be the focus of future work. Of particular interest is a recent publication by Sandoval et al. which presents a new silica-coating protocol.[62] This updated procedure is considerably more time-efficient and was shown to produce a silica shell of <5 nm in some cases. It may be possible to achieve even narrower coatings with this updated procedure.

While this simulation provides estimates regarding the sensitivity and intrinsic properties of silica coated FNDs, it does not offer insight into the mechanism behind the dramatic

https://doi.org/10.1021/acsnano.5c02407
ACS Nano 2025, 19, 36884−36895

improvement induced by the silica coating. However, given the importance of sp^2 carbon discussed above, it is hypothesized that silica may bind and passivate sp^2 carbon defects converting them to sp^3 thereby reducing the surface spin density and distribution. Another important takeaway is that the internal environment of the HPHT FNDs can support T_1 relaxation rates similar to bulk diamond with the same nitrogen content, at least in 100 nm FNDs. Future work will explore whether these relaxation rates can extend to smaller nanodiamonds where charge state dynamics and NV photostability become challenging.

Compared to other methods for extending the T_1 relaxation rate of FNDs, silica coating has a number of advantages. As shown here, it significantly improves the properties of cheap, readily available HPHT diamonds, as opposed to techniques that rely on the favorable material properties of highly expensive, CVD grown starting material, milled down to form FNDs. It is also a passive technique, compared to the use of complex pulse sequences that aim to remove the influence of noise on a measurement. This is beneficial for maintaining the simplicity of the hardware needed for sensing. On the other hand, we have shown that silica coating can increase the standoff distance between a target molecule and the embedded NV centers in diamond, therefore future work will investigate whether such improvements can be achieved using atomically thin and/or tailored surface functionalization approaches.

3. CONCLUSION

This study presents an investigation into the surface chemistry of FNDs and its impact on the spin properties of their NV ensembles. We show that oxygen functionalization of 100 nm FNDs via air oxidization and acid purification results in a small variety of oxygen functional groups, conferring a slow T_1 relaxation rate compared to commercial material. FT-IR and NEXAFS spectra were obtained after each purification step and compared to the commercial sample. The commercial sample was found to exhibit a larger proportion of aliphatic carbons (C−H stretching) compared to the oxidized samples which exhibited surfaces dominated by carboxylic acids and hydroxyl groups. NEXAFS identified potential differences in the sp^2 defect concentration which appear to correlate with the measured T_1 relaxation rates, however the sensitivity of the technique prevents a definitive link between sp^2 and the longitudinal spin relaxation rates of FNDs.

In addition to the surface termination study, we functionalized the same FND material with nanoscale silica coatings via the Stöber method. The results showed a dramatic decrease in the spin relaxation rates (increase in T_1 time), to a level commensurate with bulk diamond containing similar nitrogen concentrations. This indicates that the spin relaxation rates measured from FNDs are dominated by surface noise sources and not the bulk FND material. Additionally, we studied the relationship between chemical sensitivity and silica shell thickness using a Monte Carlo model and found that a shell thickness of approximately 1 nm is optimal to obtain maximum magnetic sensitivity.

While the current work is applied to FNDs, these surface modification and functionalization techniques can be applied to a broad range of materials hosting quantum emitters. It would be interesting to study the effects of silica coating on materials such as silicon carbide, quantum dots and group IV and V materials. This approach is an attractive alternative to complex quantum control techniques which have practical limitations for nanoscale quantum systems in the life sciences.

4. MATERIALS AND METHODS

All chemicals were purchased from Sigma-Aldrich unless otherwise stated. FT-IR spectra were recorded from 4000−400 cm^{-1} on a PE IR Spectrum ASCII PEDS 1.60 FTIR spectrometer. Spectra were acquired as the average of 8 scans using KBr pellets. The sample weight was 1.0 mg/pellet for all samples. TEM images were obtained on a transmission electron microscope (FEI Tecnai F20) operating at 200 kV. To prepare the samples, a drop of diluted colloidal solution in water:ethanol (1:1) was placed on a carbon-coated copper grid and left to dry. DLS measurements was recorded with a Zetasizer Nano ZS system (Malvern Instruments) at room temperature. Sample concentrations were 0.1 mg/mL. T_1 data was acquired on a custom-built system. NEXAFS spectra were acquired at the Australian Synchrotron, ANSTO on the soft X-ray beamline.[76]

4.1. Nanodiamond Oxidation (UoM-Ac). Nanodiamonds for the UOM-Ac sample were supplied by Microdiamant Switzerland (MSY 0−0.2) with a nominal nitrogen concentration of [N] > 100 ppm. The A-100 sample was from Adamas Nanotechnologies with product numbers NDNV100 nmHi10 mL (A-100).

The UoM samples were produced from the Microdiamant starting material by first irradiating with electrons at a fluence of 1×10^{18} electrons/cm^2, to produce lattice vacancies. This was followed by an anneal under vacuum (<1×10^{-5} mbar for the duration of the anneal, with a base pressure of 2×10^{-6} mbar) at 800 °C for 4h following by 900 °C for 1h to produce NV defects (UoM-An). Sample UoM-An was then oxidized in air using an oven furnace at different temperatures (540 °C, 550 °C, 565 °C, and 575 °C) (Supporting Information S1 and S2). To do this, a layer of nanodiamond (∼400 mg) was placed in an aluminum crucible, covered with aluminum foil and heated to temperature for 3h (UoM-AO). Following this, UoM-AO was treated with a mixture of HNO_3 and H_2SO_4 (1:3), refluxed at 90 °C for 3 days, then washed with 0.1 M NaOH for 1h at 90 °C, followed by washing with 0.1 M HCl for 1h at 90 °C. Finally, the FNDs were purified by washing/centrifugation cycles (∼5×) (until the pH neutralized), and then freeze-dried. Prior to use, the particles were dissolved in water (2 mg/mL) and sonicated in an ultrasonic bath for 30 min. The resulting transparent colloid was filtered using a 0.2 μm PVDF microfilter to provide a colloidal solution of UoM-Ac.

4.2. Silica Coated Nanodiamond. PVP (MW 10,000) was dissolved in Milli-Q water (205 mL) and sonicated for 10 min in an ultrasonic bath. UoM-Ac colloid (6 mL, 2 mg mL^{-1}) was added, and the mixture was stirred for 24 h. The colloid was then concentrated via centrifugation (10,000 rcf, 30 min) washing with Milli-Q water and the last run was washed with EtOH. Sedimented FNDs were resuspended in ethanol (12 mL) in a round-bottom flask and sonicated in an ultrasonic bath for 10 min and then TEOS was added dropwise over 10−15 min. After 2 min of vigorous stirring, ammonia solution (25%) was added dropwise over 5−10 min, and the reaction mixture was stirred for 18 h, affording UoM-Si-(1−3). The product was purified by centrifugation (10,000 rcf, 10 min) followed by washing cycles with ethanol (12 mL, 4×) and water (12 mL, 2×) and then dried under vacuum. The silica coated particles were stored in the freezer (−18 °C) as a powder.

4.3. NEXAFS. FND suspensions were drop-cast onto Au-coated Si substrates (Sigma-Aldrich) and analyzed using photon energies ranging from 270−330 eV at an X-ray incidence angle of 55°. Measurements were performed under high vacuum (<2×10^{-6} mbar) using the total electron yield (TEY) mode. Each spectrum was normalized using the "stable monitor method"[77] and further intensity normalized by setting the pre-edge to 0 and postedge to 1. Quantification of sp^2 carbon was done by taking the intensity ratios of the π^* (283.0−285.5 eV) and σ^* (289.0−320.0 eV) features and compared to a highly oriented pyrolytic graphite (HOPG) reference sample, which was also used for energy calibration.

4.4. TEM Measurements. FND suspension (0.1 μg/mL) was prepared in Milli-Q and sonicated for 15 min then drop-cast onto

https://doi.org/10.1021/acsnano.5c02407
ACS Nano 2025, 19, 36884−36895

copper-based carbon coated TEM grid (400 mesh) and let it dry. The images were taken using FEI Tecnai F20 high resolution TEM running at 200 kV.

4.5. T1 Measurement Procedure. T_1 relaxometry was performed using a custom built apparatus centered on a cuvette (BRAND 759200, Sigma-Aldrich) holding 190 μL of FNDs at 10 μg/mL. Excitation was achieved by focusing the 532 ∼ nm laser (GEM, Laser Quantum) through a 150 mm plano convex lens focused to a power density of 510 W/cm^2. Each laser pulse was performed for 120 μs to ensure optimal spin polarization. The fluorescence was time-tagged using a correlator card and binned into 10 μs windows at the beginning and end of each laser pulse to inform on the spin state population after the variable wait time τ. Fluorescence was extracted at 90° to the excitation path through a 731/137 nm band-pass filter into an optical fiber (400 μm core diameter) using an achromatic collimator with an NA of 0.54 (F950FC-A, Thorlabs). Detection was achieved using a single photon avalanche photodiode (Excelitas Technologies).

FNDs were dispersed in ultrapure water (Milli-Q, Millipore, 18.2 MΩ) for T_1 relaxation measurements. An initial baseline measurement was performed on FNDs alone, followed by a second measurement in the presence of gadobutrol monohydrate (48 mM, purchased from Sigma-Aldrich) to assess sensitivity. Gadobutrol was also prepared in Milli-Q water and added as a 10 μL volume.

Baseline T_1 relaxation curves were fitted with a stretched exponential of the form:

$$I(\tau) = C\exp(-(\Gamma_{bsl}\tau)^p) + I(\infty) \quad (2)$$

where C is the spin contrast, p is a stretch power which accounts for the variation in relaxation rates across the NV ensemble and $I(\infty)$ is the equilibrium intensity. Following the addition of Gd(III) a new measurement was taken and the effect of the target, Γ_{targ}, was determined using the following equation:

$$I(\tau) = C\exp(-(\Gamma_{bsl}\tau)^p - (\Gamma_{targ}\tau)^q) + I(\infty) \quad (3)$$

where Γ_{bsl} and p are fixed to the values obtained from the baseline measurement. All values presented were obtained from a single T_1 measurement integrated from approximately 50 min. Errors are one standard deviation in fitting error.

4.6. Monte Carlo Model. The Monte Carlo model was developed in Matlab R2020b and combined the fluorescence of 5000 FNDs containing NV defects at a density ρ. Each FND was modeled as an ellipsoid with two equal axes, a+t, with a third axis b+t, where t is the thickness of the silica shell as shown in Figure 4C). The influence of Gd(III) was determined by computing the number of ions present in a volume, V, at a given concentration, c, along with a contribution from surface adhered Gd(III) given by $n\alpha$, where α is the number of ions that would be found within a volume the same size as the given FND at this concentration and n is a multiplicative factor left as a free parameter. The volume filled by the Gd(III) was set as an ellipsoid surrounding the FND with major axes twice as large as the FND . To model Γ_{bsl}, the effective T_1 relaxation curve from the ensemble of NV defects in a sample of 5000 FNDs was computed by summing over the contributions from each individual NV defect. The T_1 relaxation rate of a given NV defect was taken as the sum of the intrinsic spin noise governedby the internal spin and phonon properties of the FND (Γ_{int} = 770 Hz), and the external surface spin noise, to give Γ_{surf}. To determine the effect of these surface spins, the distance of each NV defect from the surface of the FND was first computed. Further details of the model can be found in the Supporting Information

ASSOCIATED CONTENT

Supporting Information

The Supporting Information is available free of charge at https://pubs.acs.org/doi/10.1021/acsnano.5c02407.

Material characterization performed on two distinct batches of fluorescent nanodiamonds, with and without silica coatings. FTIR spectra, T_1 relaxation times/rates, TEM images for both batches. Experiment testing whether dissolved oxygen in water impacts the T_1 relaxation rate. NV fluorescence spectra for coated and bare FNDs. Details of the Monte Carlo model. (PDF)

AUTHOR INFORMATION

Corresponding Author

David A. Simpson − *School of Physics, The University of Melbourne, Parkville, VIC 3010, Australia;* orcid.org/0000-0001-9056-2469; Email: simd@unimelb.edu.au

Authors

Mina Barzegaramiriolya − *Bio21 Molecular Science & Biotechnology Institute and School of Chemistry, The University of Melbourne, Parkville, VIC 3010, Australia*

Erin S. Grant − *School of Physics, The University of Melbourne, Parkville, VIC 3010, Australia; School of Science, RMIT University, Melbourne, VIC 3001, Australia*

Trent Ralph − *School of Physics, The University of Melbourne, Parkville, VIC 3010, Australia*

Yang Li − *School of Chemistry, The University of Melbourne, Parkville, VIC 3010, Australia*

Giannis Thalassinos − *ARC Center of Excellence for Nanoscale BioPhotonics, School of Science and School of Science, RMIT University, Melbourne, VIC 3001, Australia*

Anton Tadich − *Australian Synchrotron, ANSTO, Clayton, VIC 3168, Australia;* orcid.org/0000-0001-9455-5901

Lars Thomsen − *Australian Synchrotron, ANSTO, Clayton, VIC 3168, Australia*

Takeshi Ohshima − *Quantum Materials and Applications Research Center, National Institutes for Quantum Science and Technology (QST), Takasaki, Gunma 3701292, Japan; Department of Materials Science, Tohoku University, Aoba-ku, Sendai 980-8579, Japan;* orcid.org/0000-0002-7850-3164

Hiroshi Abe − *Quantum Materials and Applications Research Center, National Institutes for Quantum Science and Technology (QST), Takasaki, Gunma 3701292, Japan;* orcid.org/0000-0001-9659-8382

Nikolai Dontschuk − *School of Physics, The University of Melbourne, Parkville, VIC 3010, Australia;* orcid.org/0000-0001-6061-7537

Alastair Stacey − *School of Science, RMIT University, Melbourne, VIC 3001, Australia*

Paul Mulvaney − *School of Chemistry, The University of Melbourne, Parkville, VIC 3010, Australia;* orcid.org/0000-0002-8007-3247

Liam. T. Hall − *CSIRO, Ian Wark Laboratory, Clayton, VIC 3168, Australia*

Philipp Reineck − *ARC Center of Excellence for Nanoscale BioPhotonics, School of Science and School of Science, RMIT University, Melbourne, VIC 3001, Australia;* orcid.org/0000-0003-1549-937X

Complete contact information is available at: https://pubs.acs.org/10.1021/acsnano.5c02407

Author Contributions

[$]M.B. and E.S.G. contributed equally to the work.

Notes

The authors declare the following competing financial interest(s): D.S. is a cofounder of a start-up company, FeBI

https://doi.org/10.1021/acsnano.5c02407
ACS Nano 2025, 19, 36884−36895

Technologies which commercializes quantum sensing technology. The other authors have no conflict of interest to disclose.

ACKNOWLEDGMENTS

This research was partly undertaken on the Soft X-ray Spectroscopy beamline at the Australian Synchrotron, ANSTO. The TEM images were taken at the Ian Holmes Imaging Centre, Bio21 Molecular Science and Biotechnology Institute. We acknowledge the support of the Australian Research Council (ARC) Centre of Excellence Quantum Biotechnology (CE230100021). D.S. acknowledges support via ARC Mid-Career Industry Future Fellowship (IM240100073) and the Department of Defense NSDIRG scheme (NS220100071). P.R. acknowledges support through an Australian Research Council DECRA Fellowship (grant no. DE200100279) and an RMIT University Vice-Chancellor's Senior Research Fellowship. E.S.G. acknowledges the Graeme Clark Institute for Biomedical Engineering at the University of Melbourne for funding support.

REFERENCES

(1) Childress, L.; et al. Coherent Dynamics of Coupled Electron and Nuclear Spin Qubits in Diamond. *Science* **2006**, *314*, 281−285.
(2) Cole, J. H.; Hollenberg, L. C. L. Scanning quantum decoherence microscopy. *Nanotechnology* **2009**, *20*, 495401.
(3) Miller, B. S.; et al. Spin-enhanced nanodiamond biosensing for ultrasensitive diagnostics. *Nature* **2020**, *587*, 588−593.
(4) Maze, J. R. Nanoscale magnetic sensing with an individual electronic spin in diamond. *Nature* **2008**, *455*, 644.
(5) Mochalin, V. N.; Shenderova, O.; Ho, D.; Gogotsi, Y. The properties and applications of nanodiamonds. *Nat. Nanotechnol.* **2012**, *7*, 11−23.
(6) Hsiao, W. W.-W.; Hui, Y. Y.; Tsai, P.-C.; Chang, H.-C. Fluorescent Nanodiamond: A Versatile Tool for Long-Term Cell Tracking, Super-Resolution Imaging, and Nanoscale Temperature Sensing. *Acc. Chem. Res.* **2016**, *49*, 400−407.
(7) Balasubramanian, G.; et al. Nanoscale imaging magnetometry with diamond spins under ambient conditions. *Nature* **2008**, *455*, 648−651.
(8) Barton, J.; et al. Nanoscale Dynamic Readout of a Chemical Redox Process Using Radicals Coupled with Nitrogen-Vacancy Centers in Nanodiamonds. *ACS Nano* **2020**, *14*, 12938−12950.
(9) Perona Martínez, F.; Nusantara, A. C.; Chipaux, M.; Padamati, S. K.; Schirhagl, R. Nanodiamond Relaxometry-Based Detection of Free-Radical Species When Produced in Chemical Reactions in Biologically Relevant Conditions. *ACS Sens.* **2020**, *5*, 3862−3869.
(10) Sharmin, R.; et al. Fluorescent Nanodiamonds for Detecting Free-Radical Generation in Real Time during Shear Stress in Human Umbilical Vein Endothelial Cells. *ACS Sens.* **2021**, *6*, 4349−4359.
(11) Nie, L.; et al. Quantum Sensing of Free Radicals in Primary Human Dendritic Cells. *Nano Lett.* **2022**, *22*, 1818−1825.
(12) Kucsko, G.; et al. Nanometre-scale thermometry in a living cell. *Nature* **2013**, *500*, 54−58.
(13) Simpson, D. A.; et al. Non-Neurotoxic Nanodiamond Probes for Intraneuronal Temperature Mapping. *ACS Nano* **2017**, *11*, 12077−12086.
(14) Fujiwara, M.; Shikano, Y. Diamond quantum thermometry: From foundations to applications. *Nanotechnology* **2021**, *32*, 482002.
(15) Choi, J.; et al. Probing and manipulating embryogenesis via nanoscale thermometry and temperature control. *Proc. Natl. Acad. Sci. U. S. A.* **2020**, *117*, 14636−14641.
(16) Wu, Y.; et al. Nanodiamond Theranostic for Light-Controlled Intracellular Heating and Nanoscale Temperature Sensing. *Nano Lett.* **2021**, *21*, 3780−3788.
(17) Rendler, T.; et al. Optical imaging of localized chemical events using programmable diamond quantum nanosensors. *Nat. Commun.* **2017**, *8*, 14701.
(18) Fujisaku, T.; et al. PH Nanosensor Using Electronic Spins in Diamond. *ACS Nano* **2019**, *13*, 11726−11732.
(19) Karaveli, S.; et al. Modulation of nitrogen vacancy charge state and fluorescence in nanodiamonds using electrochemical potential. *Proc. Natl. Acad. Sci. U.S.A.* **2016**, *113*, 3938−3943.
(20) Alkahtani, M. H.; et al. Fluorescent nanodiamonds: Past, present, and future. *Nanophotonics* **2018**, *7*, 1423−1453.
(21) Sotoma, S.; Okita, H.; Chuma, S.; Harada, Y. Quantum nanodiamonds for sensing of biological quantities: Angle, temperature, and thermal conductivity. *Biophys. Physicobiology* **2022**, *19*, n/a.
(22) Wu, Y.; Weil, T. Recent Developments of Nanodiamond Quantum Sensors for Biological Applications. *Adv. Sci.* **2022**, *9*. DOI: 10.1002/advs.202200059
(23) Aslam, N.; et al. Quantum sensors for biomedical applications. *Nat. Rev. Phys.* **2023**, *5*, 157−169.
(24) Ermakova, A.; et al. Detection of a few metallo-protein molecules using color centers in nanodiamonds. *Nano Lett.* **2013**, *13*, 3305−3309.
(25) Kaufmann, S.; et al. Detection of atomic spin labels in a lipid bilayer using a single-spin nanodiamond probe. *Proc. Natl. Acad. Sci. U. S. A.* **2013**, *110*, 10894−10898.
(26) Tetienne, J.; et al. Spin relaxometry of single nitrogen-vacancy defects in diamond nanocrystals for magnetic noise sensing. *Phys. Rev. B* **2013**, *87*, 235436.
(27) Norouzi, N.; et al. Relaxometry for detecting free radical generation during Bacteria's response to antibiotics. *Carbon* **2022**, *199*, 444−452.
(28) Morita, A.; et al. Detecting the metabolism of individual yeast mutant strain cells when aged, stressed or treated with antioxidants with diamond magnetometry. *Nano Today* **2023**, *48*, 101704.
(29) Li, R.; et al. Following Polymer Degradation with Nanodiamond Magnetometry. *ACS Sens.* **2022**, *7*, 123−130.
(30) Grant, E. S.; et al. Method for In-Solution, High-Throughput T 1 Relaxometry Using Fluorescent Nanodiamonds. *Phys. Rev. Appl.* **2023**, *20*, 1.
(31) March, J. E.; et al. Long spin coherence and relaxation times in nanodiamonds milled from polycrystalline ^{12}C diamond. *Phys. Rev. Appl.* **2023**, *20*, No. 044045.
(32) Oshimi, K.; et al. Bright Quantum-Grade Fluorescent Nanodiamonds. *ACS Nano* **2024**, *18* (52), 35202−35213.
(33) Joos, M. et al.. Protecting qubit coherence by spectrally engineered driving of the spin environment. *Npj Quantum Inf.* **2022**, *8*. DOI: 10.1038/s41534-022-00560-0
(34) Su, L. J. Creation of high density ensembles of nitrogen-vacancy centers in nitrogen-rich type Ib nanodiamonds. *Nanotechnology* **2013**, *24*, 315702.
(35) Ishii, S. Ensemble Negatively-Charged Nitrogen-Vacancy Centers in Type-Ib Diamond Created by High Fluence Electron Beam Irradiation. *Quantum Beam Sci.* **2022**, *6*, 2.
(36) Mrozek, M. Nitrogen-Vacancy Color Centers Created by Proton Implantation in a Diamond. *Materials* **2021**, *14*, 833.
(37) Havlik, J. et al.. Extremely rapid isotropic irradiation of nanoparticles with ions generated in situ by a nuclear reaction. *Nat. Commun.* **2018**, *9*. DOI: 10.1038/s41467-018-06789-8
(38) Acosta, V. M. et al.. Diamonds with a high density of nitrogen-vacancy centers for magnetometry applications. *Phys. Rev. B* **2009**, *80*. DOI: 10.1103/PhysRevB.80.115202
(39) Brandenburg, F.; et al. Improving the electron spin properties of nitrogen-vacancy centres in nanodiamonds by near-field etching. *Sci. Rep.* **2018**, *8*, 4−11.
(40) Cuenca, J. A.; Thomas, E.; Mandal, S.; Williams, O.; Porch, A. Microwave determination of sp2 carbon fraction in nanodiamond powders. *Carbon* **2015**, *81*, 174−178.
(41) Rosskopf, T.; et al. Investigation of surface magnetic noise by shallow spins in diamond. *Phys. Rev. Lett.* **2014**, *112*, 1−5.
(42) Ryan, R. G.; et al. Impact of Surface Functionalization on the Quantum Coherence of Nitrogen-Vacancy Centers in Nanodiamonds. *ACS Appl. Mater. Interfaces* **2018**, *10*, 13143−13149.

(43) Chakravarthi, S.; Pederson, C.; Kazi, Z.; Ivanov, A.; Fu, K. M. C. Impact of surface and laser-induced noise on the spectral stability of implanted nitrogen-vacancy centers in diamond. *Phys. Rev. B* **2021**, *104*, 1−8.
(44) Reineck, P.; et al. Effect of Surface Chemistry on the Fluorescence of Detonation Nanodiamonds. *ACS Nano* **2017**, *11*, 10924−10934.
(45) Romach, Y.; et al. Spectroscopy of surface-induced noise using shallow spins in diamond. *Phys. Rev. Lett.* **2015**, *114*, 1−5.
(46) Stacey, A.; et al. Evidence for Primal sp 2 Defects at the Diamond Surface: Candidates for Electron Trapping and Noise Sources. *Adv. Mater. Interfaces* **2019**, *6*, 1801449.
(47) Chrostoski, P.; Barrios, B.; Santamore, D. H. Magnetic field noise analyses generated by the interactions between a nitrogen vacancy center diamond and surface and bulk impurities. *Phys. B Condens. Matter* **2021**, *605*, 412767.
(48) Sangtawesin, S.; et al. Origins of Diamond Surface Noise Probed by Correlating Single-Spin Measurements with Surface Spectroscopy. *Phys. Rev. X* **2019**, *9*, 1−17.
(49) Kvakova, K.; et al. Visualization of Sentinel Lymph Nodes with Mannosylated Fluorescent Nanodiamonds. *Adv. Funct. Mater.* **2022**, DOI: 10.1002/adfm.202109960.
(50) Neburkova, J.; Vavra, J.; Cigler, P. Coating nanodiamonds with biocompatible shells for applications in biology and medicine. *Curr. Opin. Solid State Mater. Sci.* **2017**, *21*, 43−53.
(51) Nie, L.; et al. Quantum monitoring of cellular metabolic activities in single mitochondria. *Sci. Adv.* **2021**, *7*, eabf0573.
(52) Barzegar Amiri Olia, M.; Donnelly, P. S.; Hollenberg, L. C. L.; Mulvaney, P.; Simpson, D. A. Advances in the Surface Functionalization of Nanodiamonds for Biological Applications: A Review. *ACS Appl. Nano Mater.* **2021**, *4*, 9985.
(53) Suarez-Kelly, L. P.; et al. Antibody Conjugation of Fluorescent Nanodiamonds for Targeted Innate Immune Cell Activation. *Appl. Nano Mater.* **2021**, *4*, 3122−3139.
(54) Cui, C.; et al. RGDS covalently surfaced nanodiamond as a tumor targeting carrier of VEGF-siRNA: synthesis, characterization and bioassay. *J. Mater. Chem. B* **2015**, *3*, 9260−9268.
(55) Petrakova, V.; et al. Imaging of transfection and intracellular release of intact, non-labeled DNA using fluorescent nanodiamonds. *Nanoscale* **2016**, *8*, 12002−12012.
(56) Mulvaney, P.; Liz-Marzán, L. M.; Giersig, M.; Ung, T. Silica encapsulation of quantum dots and metal clusters. *J. Mater. Chem.* **2000**, *10*, 1259−1270.
(57) Jin, Y.; Kannan, S.; Wu, M.; Zhao, J. X. Toxicity of luminescent silica nanoparticles to living cells. *Chem. Res. Toxicol.* **2007**, *20*, 1126−1133.
(58) Liu, D. M.; Chen, I. W. Encapsulation of protein molecules in transparent porous silica matrices via an aqueous colloidal sol-gel process. *Acta Mater.* **1999**, *47*, 4535−4544.
(59) Kozlova, D.; et al. Cell targeting by antibody-functionalized calcium phosphate nanoparticles. *J. Mater. Chem.* **2012**, *22*, 396−404.
(60) Rehor, I.; et al. Fluorescent nanodiamonds with bioorthogonally reactive protein-resistant polymeric coatings. *ChemPlusChem.* **2014**, *79*, 21−24.
(61) Ulman, A. Formation and Structure of Self-Assembled Monolayers. *Chem. Rev.* **1996**, *96*, 1533.
(62) Sandoval, P. J.; et al. Quantum Diamonds at the Beach: Chemical insights into silica growth on nanoscale diamond using multimodal characterization and simulation. *ACS Nanosci.* **2023**, *3*, 462−474.
(63) Rehor, I.; et al. Fluorescent nanodiamonds embedded in biocompatible translucent shells. *Small* **2014**, *10*, 1106−1115.
(64) Bumb, A.; Sarkar, S. K.; Billington, N.; Brechbiel, M. W.; Neuman, K. C. Silica Encapsulation of Fluorescent Nanodiamonds for Colloidal Stability and Facile Surface Functionalization. *J. Am. Chem. Soc.* **2013**, *135*, 7815−7818.
(65) Zvi, U.; et al. Engineering spin coherence in core-shell diamond nanocrystals. *Proc. Natl. Acad. Sci. U. S. A.* **2025**, *122* (21), No. e2422542122.
(66) Wolcott, A.; et al. Surface structure of aerobically oxidized diamond nanocrystals. *J. Phys. Chem. C* **2014**, *118*, 26695−26702.
(67) Shpilman, Z.; et al. A near edge X-ray absorption fine structure study of oxidized single crystal and polycrystalline diamond surfaces. *Diam. Relat. Mater.* **2014**, *45*, 20−27.
(68) Mangolini, F.; McClimon, J. B.; Rose, F.; Carpick, R. W. Accounting for nanometer-thick adventitious carbon contamination in X-ray absorption spectra of carbon-based materials. *Anal. Chem.* **2014**, *86*, 12258−12265.
(69) Lin-Vien, D., Colthup, N. B., Fateley, W. G.; Grasselli, J. G. *The Handbook of Infrared and Raman Characteristic Frequencies of Organic Molecules*; Elsevier Science & Technology: 1991.
(70) Coates, J. Interpretation of Infrared Spectra, A Practical Approach. *Encyclopedia of Analytical Chemistry*; 2006.
(71) Reina, G.; Zhao, L.; Bianco, A.; Komatsu, N. Chemical Functionalization of Nanodiamonds: Opportunities and Challenges Ahead. *Angew. Chem. - Int. Ed.* **2019**, *58*, 17918−17929.
(72) Shenderova, O.; Nunn, N. Production and purification of nanodiamonds. *Nanodiamonds: Advanced Material Analysis, Properties and Applications*; Elsevier: 2017.
(73) Reineck, P.; et al. Not All Fluorescent Nanodiamonds Are Created Equal: A Comparative Study. *Part. Part. Syst. Charact.* **2019**, *36*, 1900009.
(74) Al-Oweini, R.; El-Rassy, H. Synthesis and characterization by FTIR spectroscopy of silica aerogels prepared using several Si(OR)4 and R″Si(OR')3 precursors. *J. Mol. Struct.* **2009**, *919*, 140−145.
(75) Eldemrdash, S.; et al. Fluorescent HPHT nanodiamonds have disk- and rod-like shapes. *Carbon* **2023**, *206*, 268−276.
(76) Cowie, B. C. C., Tadich, A.; Thomsen, L. The Current Performance of the Wide Range (90−2500 eV) Soft X-ray Beamline at the Australian Synchrotron. *AIP Conf. Proc.* **2010**, *1234*.
(77) Watts, B.; Thomsen, L.; Dastoor, P. C. Methods in carbon K-edge NEXAFS: Experiment and analysis. *J. Electron Spectrosc. Relat. Phenom.* **2006**, *151*, 105−120.

https://doi.org/10.1021/acsnano.5c02407
ACS Nano 2025, 19, 36884−36895